Single-Phase and Two-Phase Flow Through Thin and Thick Orifices in Horizontal Pipes

Manmatha K. Roul
Department of Mechanical Engineering,
Bhadrak Institute of Engineering and Technology,
Bhadrak, India 756113
e-mail: mkroul@mech.iitkgp.ernet.in

Sukanta K. Dash
Department of Mechanical Engineering,
Indian Institute of Technology,
Kharagpur, India 721302

Two-phase flow pressure drops through thin and thick orifices have been numerically investigated with air–water flows in horizontal pipes. Two-phase computational fluid dynamics (CFD) calculations, using the Eulerian–Eulerian model have been employed to calculate the pressure drop through orifices. The operating conditions cover the gas and liquid superficial velocity ranges $V_{sg} = 0.3$–4 m/s and $V_{sl} = 0.6$–2 m/s, respectively. The local pressure drops have been obtained by means of extrapolation from the computed upstream and downstream linearized pressure profiles to the orifice section. Simulations for the single-phase flow of water have been carried out for local liquid Reynolds number (Re based on orifice diameter) ranging from 3×10^4 to 2×10^5 to obtain the discharge coefficient and the two-phase local multiplier, which when multiplied with the pressure drop of water (for same mass flow of water and two phase mixture) will reproduce the pressure drop for two phase flow through the orifice. The effect of orifice geometry on two-phase pressure losses has been considered by selecting two pipes of 60 mm and 40 mm inner diameter and eight different orifice plates (for each pipe) with two area ratios ($\sigma = 0.73$ and $\sigma = 0.54$) and four different thicknesses ($s/d = 0.025$–0.59). The results obtained from numerical simulations are validated against experimental data from the literature and are found to be in good agreement. [DOI: 10.1115/1.4007267]

1 Introduction

The calculation of pressure drop due to gas-liquid two-phase flow through an orifice is a problem yet to be solved in engineering design. Knowledge of pressure drop for two-phase flows through valves, orifices, and other pipe fittings are important for the control and operation of industrial devices, such as chemical reactors, power generation units, refrigeration apparatuses, oil wells, and pipelines. The orifice is one of the most commonly used elements in flow rate measurement and regulation. Because of its simple structure and reliable performance, the orifice is increasingly adopted in gas-liquid two-phase flow measurements. Single orifices or arrays of them constituting perforated plates, are often used to enhance flow uniformity and mass distribution downstream of manifolds and distributors. They are also used to enhance the heat-mass transfer in thermal and chemical processes (e.g., distillation trays). Single-phase flows across orifices have been extensively studied, as has been shown by Idelchik et al. [1] in their handbook. The available correlations do not always take into account Reynolds number effect and a complete set of geometrical parameters. Some investigations have been made on the theory and experiment of resistance characteristics of orifices [1–7] and some useful correlations have been proposed. However, some of them cover only a limited range of operating conditions, and the errors of some are far beyond the limit of tolerance. So they are not widely used in engineering design. Major uncertainties exist with reference to two-phase flows through orifices. Few experimental studies reported in the literature often refer to a limited set of operating conditions. With particular reference to orifice plates, some of the correlations and models [2–4] are discussed by Friedel [5]. Other references are the early study by Janssen [6] on two-phase pressure loss across abrupt area contractions and expansions taking steam water flow, the work by Lin [7] on two-phase flow measurement with sharp edge orifices; the recent experimental investigation by Saadawi et al. [8], which refers to two-phase flows across orifices in large diameter pipes and the work by Kojasoy et al. [9] on multiple thick and thin orifice plates. Bertola [10] studied void fraction distribution for air–water flow in a horizontal test section with sudden area contraction and found that the sudden contraction considerably affects the gas distribution in both the upstream and the downstream pipe. Fossa and Guglielmini [11], Fossa et al. [12], and Jones and Zuber [13] experimentally investigated two-phase flow pressure drop through thin and thick orifices and observed that the void fraction generally increases across the singularity and attains a maximum value just downstream of restriction. Shedd and Newell [14] found a unique set of liquid film thickness and pressure drop data for horizontal, annular flow of air and water through round, square and triangular tube using a noninvasive, optical liquid film thickness measurement system.

The information regarding the effects of orifice thickness on two-phase pressure losses is not available in the literature. Most models require the knowledge of local void fraction, which is usually calculated by means of correlations for straight pipes without orifices and hence the actual void fraction distribution due to orifice interactions is not considered. In the present study the effect of orifice geometry on two-phase pressure losses has been considered by selecting two pipes of 60 mm and 40 mm inner diameter and eight different orifice plates (for each pipe) with two area ratios ($\sigma = 0.73$ and $\sigma = 0.54$) and four different thicknesses (three thin and one thick orifice) ($s/d = 0.025$, 0.05, 0.2, 0.59). When the value of s/d is below 0.5 it is called a thin orifice otherwise it is a thick orifice [3]. The results presented in this study provide useful information on the reliability of available models and correlations when applied to intermittent flows through orifices having high values of the contraction area ratio.

2 Theoretical Background

2.1 Single-Phase Flow. For the flow through a thin orifice (Fig. 1(*a*)), the flow contracts with negligible losses of mechanical energy, to a vena contracta of area A_c that forms outside the restriction. Downstream of the vena contracta the flow expands in an irreversible process to the pipe wall of flow area A. If the

Contributed by the Fluids Engineering Division of ASME for publication in the Journal of Fluid Engineering. Manuscript received January 23, 2012; final manuscript received July 14, 2012; published online August 21, 2012. Assoc. Editor: John Abraham.

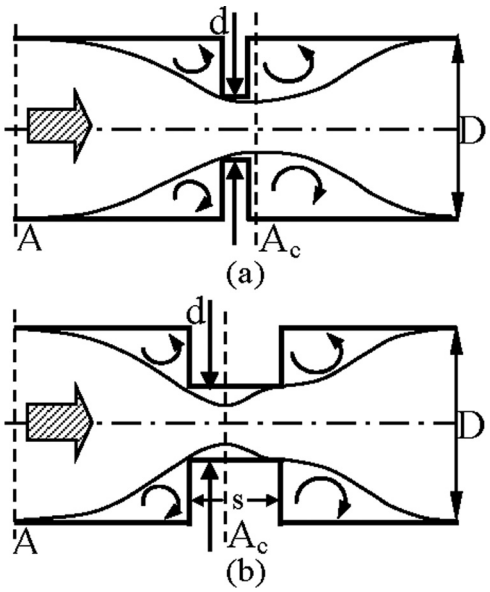

Fig. 1 Single-phase flow across (*a*) thin and (*b*) thick orifices

orifice is thick (Fig. 1(*b*)), downstream of the vena contracta, the flow reattaches to the wall within the length of the geometrical contraction and can even develop a boundary layer flow until it finally expands back into the pipe wall. According to Chisholm [3], the thick orifice behavior takes place when the dimensionless orifice thickness to diameter ratio, s/d is greater than 0.5. Assuming that each expansion occurs irreversibly and the fluid is incompressible, the single-phase pressure drop ΔP_{sp} in a thin orifice can be expressed as a function of the flow area ratio $\sigma = (d/D)^2$ and the contraction coefficient $\sigma_c = A_c/A\sigma$ as

$$\Delta P_{sp} = \frac{\rho V^2}{2}\left[\left(\frac{1}{\sigma\sigma_c} - 1\right)\right]^2 \tag{1}$$

where ρ is the fluid density and V its mean velocity.

If the orifice is thick, the loss of mechanical energy is due to the double expansion as described above. For these conditions the single-phase overall pressure drop can be expressed as

$$\Delta P_{sp} = \frac{\rho V^2}{2}\left[\left(\frac{1}{\sigma\sigma_c}\right)^2 - 1 - \frac{2}{\sigma^2}\left(\frac{1}{\sigma_c} - 1\right) - 2\left(\frac{1}{\sigma} - 1\right)\right] \tag{2}$$

The local pressure drop can also be expressed as a function of orifice discharge coefficient C_d (Lin [7], Grace and Lapple [15]),

$$\Delta P_{sp} = \frac{\rho V^2}{2}\left[\left(\frac{1}{\sigma}\right)^2 - 1\right]\frac{1}{C_d^2} \tag{3}$$

From Eqs. (1) and (3), σ_c for thin orifices can be written as

$$\sigma_{c,\text{thin}} = \frac{1}{\sigma + \sqrt{1 - \sigma^2}/C_d} \tag{4}$$

Similarly from Eqs. (2) and (3), σ_c for thick orifices can be written as

$$\sigma_{c,\text{thick}} = \frac{1}{1 + \sqrt{\left[(1 - \sigma^2)/C_d^2\right] - 1 + 2\sigma - \sigma^2}} \tag{5}$$

The well-known Chisholm expression for contraction coefficient in terms of the area flow ratio only (Chisholm [3], Bullen et al. [16], and Benedict [17]) is given as

$$\sigma_c = \frac{1}{\left[0.639(1 - \sigma)^{0.5} + 1\right]} \tag{6}$$

In the present study the pressure drops across different orifices for single phase flow of water are obtained numerically, from which the discharge coefficient is calculated using Eq. (3). The contraction coefficient is calculated using Eqs. (4) and (5) for thin and thick orifices, respectively. This contraction coefficient is compared with the Chisholm correlation as given by Eq. (6).

2.2 Two-Phase Flow. According to Chisholm [3] and Morris [4], the slip ratio S is defined as the ratio of gas phase velocity to the liquid phase velocity at any point in the flow path (Collier and Thome [18]) and it is a function of the quality x and the ratio of fluid densities. When the quality of mixtures, x is very low (such as those considered in the present investigation, $x < 0.005$), the slip ratio, S can be expressed as

$$S = \left[1 + x\left(\frac{\rho_l}{\rho_g} - 1\right)\right]^{0.5} \tag{7}$$

The quality, x is defined as the ratio of mass flux of gas to the total mass flux of mixture at any cross section [18]. The mass flux of gas is the gas mass flow rate divided by total cross-sectional area of pipe, whereas the total mass flux is the total mass flow rate of mixture divided by total cross-sectional area of the pipe. Mathematically the quality x can be expressed as

$$x = \frac{\rho_g g V_{sg}/A_{\text{cross}}}{\rho_g g V_{sg}/A_{\text{cross}} + \rho_l g V_{sl}/A_{\text{cross}}} = \frac{\rho_g V_{sg}}{\rho_g V_{sg} + \rho_l V_{sl}} \tag{8}$$

The Armand and Threschev correlation [19] for fully developed flow, near atmospheric pressure, can be expressed in terms of the gas volume fraction $x_v = V_{sg}/(V_{sg} + V_{sl})$,

$$S = \frac{1 - 0.833x_v}{0.833(1 - x_v)} \tag{9}$$

Kojasoy et al. [9] adopted the Chisholm expression for slip ratio S but they suggest a correction to account for the effect of flow restriction on slip ratio,

$$S = \left[\left\{1 + x\left(\frac{\rho_l}{\rho_g} - 1\right)\right\}^{0.5}\right]^n \tag{10}$$

The exponent n is zero at the vena contracta and downstream of it (i.e., the slip ratio is expected to be one) while n is equal to 0.4 and 0.15 in the upstream region for thin and thick orifices, respectively.

Simpson et al. [2] adopted a different correlation for slip evaluation that does not account for the quality of the mixture,

$$S = \left(\frac{\rho_l}{\rho_g}\right)^{1/6} \tag{11}$$

The prediction of the two-phase multiplier Φ_{lo}^2 can be calculated using different models as described below. The two-phase multiplier is defined as the ratio of the two-phase pressure drop through the orifice to the single-phase pressure drop obtained at liquid mass flux equal to the overall two-phase mass flux.

If the mixture is considered homogeneous ($S = 1$), the following expression can be obtained:

$$\Phi_{lo}^2 = \frac{\rho_l}{\rho_g}x + (1 - x) \tag{12}$$

Chisholm [3] developed the following expression:

$$\Phi_{lo}^2 = 1 + \left(\frac{\rho_l}{\rho_g} - 1\right)\left[Bx(1-x) + x^2\right] \tag{13}$$

where the parameter B can be assumed to be 0.5 for thin orifices and 1.5 for thick ones.

The Morris relationship [4] refers to thin orifices and gate valves and has the following expression:

$$\Phi_{lo}^2 = \left[x\frac{\rho_l}{\rho_g} + S(1-x)\right]\left[x + \left(\frac{1-x}{S}\right)\left(1 + \frac{(S-1)^2}{\left(\rho_l/\rho_g\right)^{0.5} - 1}\right)\right] \tag{14}$$

where, the slip ratio S is given by Eq. (7).

Simpson et al. [2] proposed the following relationship based on slip predictions given by Eq. (11):

$$\Phi_{lo}^2 = [1 + x(S-1)]\left[1 + x\left(S^5 - 1\right)\right] \tag{15}$$

The Simpson model is based on data collected with large diameter pipes (up to 127 mm) at mixture qualities generally higher than those obtained in this work ($x < 0.005$).

Finally the correlation of Saadawi et al. [8], based on experiments carried out at near atmospheric pressure with a very large diameter pipe (203 mm), is given by

$$\Phi_{lo}^2 = 1 + 184x - 7293x^2 \tag{16}$$

In the present study the pressure drops across different orifices for two-phase flow of air-water mixtures are obtained numerically. The single-phase pressure drops at liquid mass flux equal to the overall two-phase mass flux are obtained by interpolating the single-phase pressure drop results. The two-phase multiplier is obtained by taking the ratio of the two-phase pressure drop to that of the single phase pressure drop. The two-phase multiplier thus obtained is compared with the theoretical predictions from the above equations (Eqs. (12)–(16)).

3 Numerical Modeling

The flow field is modeled using the averaged Reynolds equations with realizable per-phase k-ε turbulence model, with the two layer near-wall treatment. The governing equations are briefly described below.

3.1 Governing Equations. Here we considered the two-fluid method or Eulerian–Eulerian model, which considers both the phases as interpenetrating continuum, with each computational cell of the domain containing respective fractions of the continuous and dispersed phases. We have adopted the following assumptions in our study which are very realistic for the present situation.

Assumptions:

1. The fluids in both phases are Newtonian, viscous and incompressible.
2. The physical properties remain constant.
3. No mass transfer between the two phases.
4. The pressure is assumed to be common to both the phases.
5. The realizable k-ε turbulent model is applied to describe the behavior of each phase.
6. The surface tension forces are neglected; therefore, the pressures of both phases are equal at any cross section.
7. The flow is assumed to be isothermal, so the energy equations are not needed.

With all the above assumptions the governing equations for phase q can be written as (Drew [20], Drew and Lahey [21], Crowe et al. [22]):

Continuity equation:

$$\frac{\partial}{\partial t}\left(\alpha_q \rho_q\right) + \nabla \cdot \left(\alpha_q \rho_q \vec{v}_q\right) = 0 \tag{17}$$

The volume fractions are assumed to be continuous functions of space and time and their sum is equal to one

$$\alpha_q + \alpha_p = 1 \tag{18}$$

Momentum equation:

$$\frac{\partial}{\partial t}\left(\alpha_q \rho_q \vec{v}_q\right) + \nabla \cdot \left(\alpha_q \rho_q \vec{v}_q \vec{v}_q\right) = -\alpha_q \nabla p + \nabla \cdot \left(\bar{\bar{\tau}}_q\right) + \alpha_q \rho_q \vec{g} + M_q \tag{19}$$

$\bar{\bar{\tau}}_q$, is the qth phase stress tensor

$$\bar{\bar{\tau}}_q = \alpha_q \mu_q^{\text{eff}}\left(\nabla \vec{v}_q + \nabla \vec{v}_q^T\right) \tag{20}$$

$$\mu_q^{\text{eff}} = \mu_q + \mu_{t,q} \tag{21}$$

where M_q is the interfacial momentum transfer term, which is given by

$$M_q = M_q^d + M_q^{VM} + M_q^L \tag{22}$$

where the individual terms on the right-hand side of Eq. (22) are the drag force, virtual mass force, and lift force, respectively. The drag force is expressed as

$$M_q^d = \frac{3}{4d_p}\alpha_p \rho_q C_D \left|\vec{v}_p - \vec{v}_q\right|\left(\vec{v}_p - \vec{v}_q\right) \tag{23}$$

The drag coefficient C_D depends on the particle Reynolds number as given below (Wallis [23]),

$$\begin{aligned} C_D &= 24\left(1 + 0.15\ \text{Re}^{0.687}/\text{Re}_p\right) && \text{Re}_p \le 1000 \\ &= 0.44 && \text{Re}_p > 1000 \end{aligned} \tag{24}$$

Particle Reynolds number for primary phase q and secondary phase p is given by

$$\text{Re}_p = \frac{\rho_q \left|\vec{v}_q - \vec{v}_p\right| d_p}{\mu_q} \tag{25}$$

Equation (23) shows that the drag force exerted by the secondary phase (bubbles) on the primary phase is a vector directed along the relative velocity of the secondary phase. We have varied the diameter of the particle from 10 to 100 micron and have not seen any change in the pressure profile within this range of diameter change.

The second term in Eq. (22) represents the virtual mass force, which comes into play when one phase is accelerating relative to the other one. In case of bubble accelerating in a continuous phase, this force can be described by the following expression [20]:

$$M_q^{VM} = -M_p^{VM} = C_{VM}\alpha_p \rho_q \left(\frac{d_q \vec{v}_q}{dt} - \frac{d_p \vec{v}_p}{dt}\right) \tag{26}$$

where C_{VM} is the virtual mass coefficient, which for a spherical particle is equal to 0.5 [20].

The third term in Eq. (22) is the lift force, which arises from a velocity gradient of the continuous phase in the lateral direction and is given by Drew and Lahey [21],

$$M_q^L = -M_p^L = C_L \alpha_p \rho_q \left(\vec{v}_p - \vec{v}_q\right) \times \left(\nabla \times \vec{v}_q\right) \tag{27}$$

where C_L is the lift force coefficient, which for shear flow around a spherical droplet is equal to 0.5.

Turbulence modeling:

Here we considered the realizable per-phase k-ε turbulence model (Launder and Spalding [24], Shih et al. [25], Troshko and Hassan [26]).

Transport equations for k:

$$\begin{aligned}\frac{\partial}{\partial t}\left(\alpha_q\rho_q k_q\right)+\nabla.\left(\alpha_q\rho_q\overrightarrow{U}_q k_q\right)&=\nabla.\left[\alpha_q\left(\mu_q+\frac{\mu_{t,q}}{\sigma_k}\right)\nabla k_q\right]+\left(\alpha_q G_{k,q}-\alpha_q\rho_q\varepsilon_q\right)\\&+K_{pq}\left(C_{pq}k_p-C_{qp}k_q\right)-K_{pq}\left(\overrightarrow{U}_p-\overrightarrow{U}_q\right).\frac{\mu_{t,p}}{\alpha_p\sigma_p}\nabla\alpha_p\\&+K_{pq}\left(\overrightarrow{U}_p-\overrightarrow{U}_q\right).\frac{\mu_{t,q}}{\alpha_q\sigma_q}\nabla\alpha_q\end{aligned}\tag{28}$$

Transport equations for ε:

$$\begin{aligned}\frac{\partial}{\partial t}\left(\alpha_q\rho_q\varepsilon_q\right)+\nabla.\left(\alpha_q\rho_q\overrightarrow{U}_q\varepsilon_q\right)&=\nabla.\left[\alpha_q\left(\mu_q+\frac{\mu_{t,q}}{\sigma_\varepsilon}\right)\nabla\varepsilon_q\right]+\alpha_q\rho_q C_1 S\varepsilon_q-C_2\alpha_q\rho_q\frac{\varepsilon_q^2}{k_q+\sqrt{\nu_{t,q}\varepsilon_q}}\\&+C_{1\varepsilon}\frac{\varepsilon_q}{k_q}\left[K_{pq}\left(C_{pq}k_p-C_{qp}k_q\right)-K_{pq}\left(\vec{U}_p-\vec{U}_q\right)\cdot\frac{\mu_{t,p}}{\alpha_p\sigma_p}\nabla\alpha_p\right.\\&\left.+K_{pq}\left(\vec{U}_p-\vec{U}_q\right)\cdot\frac{\mu_{t,q}}{\alpha_q\sigma_q}\nabla\alpha_q\right]\end{aligned}\tag{29}$$

where $\vec{U}_q$ is the phase-weighted velocity. Here,

$$C_1=\max\left[0.43,\frac{\eta}{\eta+5}\right],\quad \eta=S\frac{k}{\varepsilon},\quad S=\left(2S_{ij}S_{ij}\right)^{0.5}$$

The terms C_{pq} and C_{qp} can be approximated as

$$C_{pq}=2,\quad C_{qp}=2\left(\frac{\eta_{pq}}{1+\eta_{pq}}\right)\tag{30}$$

where η_{pq} is defined as

$$\eta_{pq}=\frac{\tau_{t,pq}}{\tau_{F,pq}}\tag{31}$$

where the Lagrangian integral time scale ($\tau_{t,pq}$), is defined as

$$\tau_{t,pq}=\frac{\tau_{t,q}}{\sqrt{\left(1+C_\beta\xi^2\right)}}\tag{32}$$

where

$$\xi=\frac{\left|\vec{v}_{pq}\right|\tau_{t,q}}{L_{t,q}}\tag{33}$$

where $\tau_{t,q}$ is a characteristic time of the energetic turbulent eddies and is defined as

$$\tau_{t,q}=\frac{3}{2}C_\mu\frac{k_q}{\varepsilon_q}\tag{34}$$

and

$$C_\beta=1.8-1.35\cos^2\theta\tag{35}$$

where θ is the angle between the mean particle velocity and the mean relative velocity. The characteristic particle relaxation time connected with inertial effects acting on a dispersed phase p is defined as

$$\tau_{F,pq}=\alpha_p\rho_q K_{pq}^{-1}\left(\frac{\rho_p}{\rho_q}+C_V\right)\tag{36}$$

where $C_V=0.5$

K_{pq} is defined as the inter phase momentum exchange coefficient. In flows where there are unequal amounts of two fluids, the predominant fluid is modeled as the primary fluid, since the sparser fluid is more likely to form droplets or bubbles. The exchange coefficient for these types of bubbly, liquid-liquid or gas-liquid mixtures can be written in the following general form:

$$K_{pq}=\frac{\propto_q\propto_p\rho_p f}{\tau_p}$$

where f, the drag function, is defined differently for the different exchange-coefficient models and τ_p, the "particulate relaxation time," is defined as

$$\tau_p=\frac{\rho_p d_p^2}{18\mu_q}$$

where d_p is the diameter of the bubbles or droplets of phase p.

The eddy viscosity model is used to calculate averaged fluctuating quantities. The Reynolds stress tensor for continuous phase q is given as

$$\bar{\bar{\tau}}_q=-\frac{2}{3}\left(\rho_q k_q+\rho_q\mu_{t,q}\nabla\cdot\vec{U}_q\right)\bar{\bar{I}}+\rho_q\mu_{t,q}\left(\nabla\vec{U}_q+\nabla\vec{U}_q^T\right)\tag{37}$$

The turbulent viscosity $\mu_{t,q}$ is written in terms of the turbulent kinetic energy of phase q,

$$\mu_{t,q}=\rho_q C_\mu\frac{k_q^2}{\varepsilon_q}\tag{38}$$

The production of turbulent kinetic energy, $G_{k,q}$ is computed from

$$G_{k,q}=\mu_{t,q}\left(\nabla\vec{v}_q+\nabla\vec{v}_q^T\right):\nabla\vec{v}_q\tag{39}$$

The production term in the ε equation (the second term on the right-hand side of Eq. (29)) does not contain the same G_k term as the other k-ε models. Another desirable feature in the realizable k-ε model is that the destruction term (the third term on the right-hand side of Eq. (29)) does not have any singularity, i.e., its denominator never vanishes, even if k vanishes or become smaller than zero. This feature is contrasted with traditional k-ε models, which have a singularity due to k in denominator. Unlike standard and RNG k-ε models, C_μ is not a constant here. It is computed from

$$C_\mu=\frac{1}{A_0+A_s\frac{kU^*}{\varepsilon}}\tag{40}$$

where

$$U^*\equiv\sqrt{S_{ij}S_{ij}+\tilde{\Omega}_{ij}\tilde{\Omega}_{ij}}\tag{41}$$

and

$$\tilde{\Omega}_{ij}=\Omega_{ij}-2\varepsilon_{ijk}\omega_k$$

$$\Omega_{ij}=\overline{\Omega_{ij}}-\varepsilon_{ijk}\omega_k$$

where, $\overline{\Omega_{ij}}$ is the mean rate of rotation tensor viewed in a rotating reference frame with the angular velocity $\overline{\omega_k}$. The constants A_0 and A_s are given by

$$A_0 = 4.04, \quad A_s = \sqrt{6}\cos\phi$$

where $\phi = \frac{1}{3}\cos^{-1}(\sqrt{6}W)$, $W = \frac{S_{ij}S_{jk}S_{ki}}{\tilde{S}^3}$, $\tilde{S} = \sqrt{S_{ij}S_{ij}}$, $S_{ij} = \frac{1}{2}\left(\frac{\partial u_j}{\partial x_i} + \frac{\partial u_i}{\partial x_j}\right)$.

The constants used in the model are the following:

$$C_{1\varepsilon} = 1.44, \quad C_2 = 1.9, \quad \sigma_k = 1.0, \quad \sigma_\varepsilon = 1.2$$

Interphase turbulent momentum transfer:

The turbulent drag term $K_{pq}(\vec{v}_p - \vec{v}_q)$ is modeled as follows:

$$K_{pq}(\vec{v}_p - \vec{v}_q) = K_{pq}(\vec{U}_p - \vec{U}_q) - K_{pq}\vec{v}_{dr,pq} \tag{42}$$

Here $\vec{U}_p$ and $\vec{U}_q$ are phase-weighted velocities, and $\vec{v}_{dr,pq}$ is the drift velocity for phase p, which is computed as follows:

$$\vec{v}_{dr,pq} = -\left(\frac{D_p}{\sigma_{pq}\alpha_p}\nabla\alpha_p - \frac{D_q}{\sigma_{pq}\alpha_q}\nabla\alpha_q\right) \tag{43}$$

The diffusivities D_p and D_q are computed directly from the transport equations. The drift velocity results from turbulent fluctuations in the volume fraction. When multiplied by the exchange coefficient K_{pq} it serves as a correction to the momentum exchange term for turbulent flows.

3.2 Boundary Conditions. Velocity inlet boundary condition is applied at the inlet (as shown in Fig. 2). A no-slip and no-penetrating boundary condition is imposed on the wall of the pipe and the two-layer model for enhanced wall treatment was used to account for the viscosity-affected near-wall region. At the outlet, the boundary condition is assigned as outflow, which implies diffusion flux for the entire variables in exit direction are zero. Symmetry boundary condition is considered at the axis, which implies normal gradients of all flow variables are zero and radial velocity and the shear stress are zero at the axis.

Boundary conditions for k and ε at the inlet are taken as

$$k = \frac{1}{2}(0.02 \times \text{inlet velocity})^2$$

$$\varepsilon = \frac{0.09 \times k^2}{10 \times \text{laminar viscosity}}$$

3.3 Near-Wall Treatment. The two-layer model for enhanced wall treatment was used to account for the viscosity-affected near-wall region in numerical computation of turbulent flow. The whole domain is subdivided into a viscosity affected region and a fully turbulent region. The demarcation of the two regions is determined by a wall distance based turbulent Reynolds number, Re_y defined as

$$\mathrm{Re}_y = \frac{\rho y\sqrt{k}}{\mu} \tag{44}$$

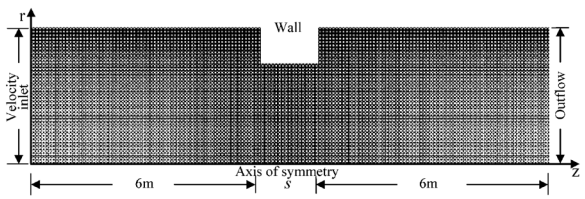

Fig. 2 Computational domain for $\sigma = 0.54$, $s/d = 0.20$, $D = 40$ mm

where, y is the normal distance from the wall at the cell centers and it is interpreted as the distance to the nearest wall,

$$y = \min_{\vec{r}_w \in \Gamma_w} \|\vec{r} - \vec{r}_w\| \tag{45}$$

where $\vec{r}$ is the position vector at field point, and $\vec{r}_w$ is the position vector on the wall boundary. Γ_w is the union of all the wall boundaries involved. This interpretation allows y to be uniquely defined in flow domains of complex shape involving multiple walls.

In the fully turbulent region ($\mathrm{Re}_y > \mathrm{Re}_y^*, \mathrm{Re}_y^* = 200$), the k-ε models are employed (Launder and Spalding [24]). In the viscosity affected near wall region ($\mathrm{Re}_y < \mathrm{Re}_y^*$), the one-equation model of Wolfstein [27] is employed. In one equation model, the momentum equations and k equation are retained. However, the turbulent viscosity, μ_t is computed from

$$\mu_{t,2\text{layer}} = \rho C_\mu l_\mu \sqrt{k} \tag{46}$$

while the rate of dissipation of turbulent kinetic energy ε is computed from

$$\varepsilon = \frac{k^{3/2}}{l_\varepsilon} \tag{47}$$

The length scales l_μ and l_ε in Eqs. (46) and (47) are computed from Chen and Patel [28],

$$l_\mu = y c_l (1 - e^{-\mathrm{Re}_y/A_\mu}) \tag{48}$$

$$l_\varepsilon = y c_l \left(1 - e^{-\mathrm{Re}_y/A_\varepsilon}\right) \tag{49}$$

Here, the two-layer definition is smoothly blended with the high Reynolds number μ_t definition (as described in the k-ε models) from the outer region,

$$\mu_{t,\text{enh}} = \lambda_\varepsilon \mu_t + (1 - \lambda_\varepsilon)\mu_{t,2\text{layer}} \tag{50}$$

A blending function λ_ε is defined in such a way that it is equal to unity far from the walls and is zero very near to the walls,

$$\lambda_\varepsilon = \frac{1}{2}\left[1 + \tanh\left(\frac{\mathrm{Re}_y - \mathrm{Re}_y^*}{A}\right)\right] \tag{51}$$

The constant A determines the width of the blending function. By defining a width such that the value of λ_ε will be within 1% of its far field value given by a variation of $\Delta\mathrm{Re}_y$,

$$A = \frac{|\Delta\mathrm{Re}_y|}{\tanh(0.98)} \tag{52}$$

The constants are $c_l = kC_\mu^{-3/4}, A_\mu = 70, A_\varepsilon = 2c_l$

3.4 Numerical Schemes. The governing equations of mass, momentum, and turbulent quantities have been integrated over a control volume and the subsequent equations have been discretized over the control volume using the finite volume technique (Patankar [29]) to yield a set of algebraic equations. Boundary conditions were implemented to the finite volume equations which could be solved by the algebraic multigrid scheme of Fluent 6.3. The flow field was assumed to be axisymmetric and solved in two dimensions. The algebraic equations were solved using double precision solver with an implicit scheme for all variables with a variable time step starting at 0.00001 s and finally going up to 0.001 s for quick convergence. The discretization scheme for momentum, volume fraction, turbulent kinetic energy and

turbulent dissipation rate were taken to be first order up winding initially for better convergence. Slowly as time progressed the discretization forms were switched over to second order up winding and then slowly towards the QUICK scheme for better accuracy. It is to be noted here that in the Eulerian scheme of solution, two continuity equations and two momentum equations were solved for two phases. The phase-coupled SIMPLE algorithm (Vasquez and Ivanov [30], Ansari and Shokri [31]) which is an extension of the SIMPLE algorithm (Patankar [29]) for multiphase flows was used for the pressure-velocity coupling. The velocities were solved coupled by the phases, but in a segregated fashion. The block algebraic multigrid (AMG) method (Wesseling [32], Weiss et al. [33]) was used to solve all the algebraic equations resulting from the discretization of the continuity and momentum equations of all phases simultaneously. Then a pressure correction equation was built based on total volume continuity rather than mass continuity. Pressure and velocities were then corrected so as to satisfy the continuity constraint. The realizable per-phase k-ε model (Shih et al. [25]) has been used as a closure model for turbulent flow. The two-layer model for enhanced wall treatment was used to account for the viscosity-affected near-wall region in numerical computation of turbulent flow. Fine grids were used near the wall as well as near the orifice, where the mean flow changes rapidly and there are shear layers with a large mean rate of strain. The scaled residuals for continuity, velocity of water and air in axial and radial directions, k and ε for water and air, and volume fraction for air were monitored. The convergence criteria for all the variables were taken to be 0.001. If the residuals for all problem variables fall below the convergence criteria but are still in decline, the solution is still changing, to a greater or lesser degree. A solution is said to be truly converged if the scaled residuals are no longer changing with successive iterations. A better indicator occurs when the residuals flatten in a traditional residual plot (of residual value versus iteration). Convergence was judged not only by examining scaled residual levels, but also by monitoring the velocities and pressures at three different locations very close to the orifice section (at 5D upstream, at the orifice and at 5D downstream). The solution was considered to have converged when there was no further observable change in the velocity and pressure at each location. Finally it was observed that the scaled residual for continuity equation was below 10^{-3} and that for all other variables were well below 10^{-6}. The convergence criteria were selected by first solving the problem in transient state and then it is solved in steady state.

3.5 Grid Independence Study. In order to determine the proper grid size for this study, a grid independence test was conducted for the Reynolds number of 100000, area ratio of 0.54, orifice thickness to diameter ratio of 0.20 in 40 mm diameter pipe. Five different grid densities were used for the grid independence study. Figure 3 shows the dependence of ΔP on the grid size. A comparison of the predicted pressure drop values among the five different cases suggests that the three cell distributions of 236640, 473280, and 946560 give nearly identical results. Considering both the accuracy and computational time, the calculations were all performed with 236640 cells (inlet section-880 × 132, orifice-60 × 72, and outlet section-880 × 132) for this case. Figure 2 shows the domain used for the area ratio of 0.54, orifice thickness to diameter ratio of 0.20 in 40 mm diameter pipe (half of the section is modeled, with a symmetry boundary at the centerline). Similarly the numerical mesh used for different values of s/d, area ratio and pipe diameter, were determined from several numerical experiments which showed that further refinement in grids in either direction did not change the result (maximum change in pressure drop or any scalar variable) by more than 2%.

4 Results and Discussions

Two different horizontal pipes are considered, having inner diameters D equal to 60 mm and 40 mm. The test section is about

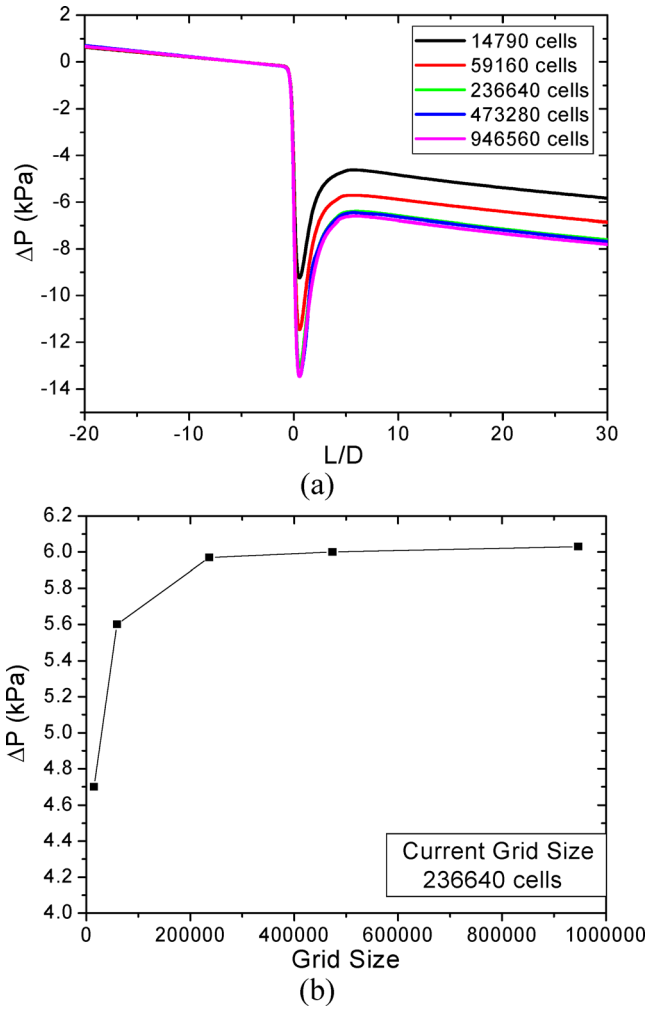

Fig. 3 Axial pressure drop at the orifice section as a function of grid size. (*a*) Pressure profile, (*b*) pressure drop (Re = 100,000, $\sigma = 0.54$, $s/d = 0.20$, $D = 40$ mm).

12 m long. The orifice is located 6 m downstream the inlet section. The effect of orifice geometry has been considered by selecting 16 different orifices. The 16 shapes here result from two pipe diameters ($D = 60$ mm and 40 mm), two area ratios ($\sigma = 0.73$ and 0.54) and four orifice thicknesses ($s/d = 0.025$, 0.05, 0.20, and 0.59). According to Chisholm [3] criteria the orifice having $s/d = 0.59$ can be classified as a "thick" orifice. The fluids used are air and water at room temperature and near atmospheric pressure. Gas superficial velocities are taken in the range $V_{sg} = 0.3$–4 m/s, while liquid superficial velocities are taken in the range $V_{sl} = 0.6$–2 m/s.

The local pressure drops have been obtained by extrapolating the computed pressure profiles upstream and downstream of the orifice (in the region of fully developed pipe flow) to the orifice section as demonstrated in Fig. 4. For fully developed flow in upstream and downstream of the orifice section the variation of static pressure with length of the pipe (L/d) is linear. These linearized pressure profiles are extrapolated to the orifice section as shown in Fig. 4, from which the pressure drop at the orifice section is calculated. Local pressure drop means the pressure drop at the orifice section.

The reference pressure is located at a distance of $5d$ from the orifice section in the upstream direction, where d is the diameter of the orifice. The pressure at this location is taken as the atmospheric pressure or zero gauge pressure. If the pressure at any section is more than the reference pressure then it is positive or else it is negative as can be seen from Fig. 4. The position of the orifice

is taken as the origin and the upstream distances are taken as negative, whereas the downstream distances are taken as positive. The procedure is repeated for single-phase flow of water and two-phase flow of air-water mixtures in order to compute the two-phase multiplier Φ_{lo}^2.

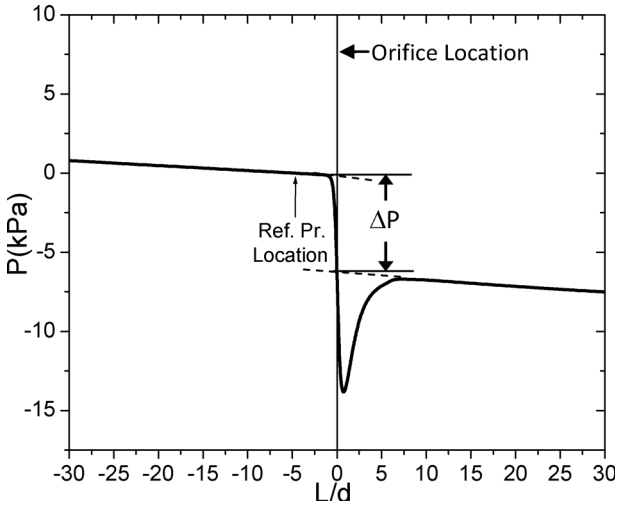

Fig. 4 Local pressure drop at the orifice section by extrapolating the upstream and downstream computed pressure profiles to the orifice section

4.1 Single-Phase Flow. The velocity vectors and streamlines for single phase water flow through orifices having $s/d = 0.025$, 0.2, and 0.59 are shown in Figs. 5, 6, and 7, respectively. It is evident from the figures that for the flow through thin orifices ($s/d = 0.025$, 0.2), the flow contracts to a vena contracta that forms outside the restriction. At the vena contracta the flow becomes parallel and downstream of the vena contracta the flow expands to the pipe wall of flow area A. A region of separated flow occurs from the sharp corner of the orifice and extends past the vena contracta. For the flow through thick orifice ($s/d = 0.59$), vena contracta always forms inside the restriction. Downstream of the vena contracta, the flow reattaches to the wall within the length of the geometrical contraction and it finally expands back into the pipe wall. Simulated velocity vectors clearly show that eddy zones are formed in the separated flow region. The pressure profiles for the single phase flow of water through orifices of different thicknesses in 40 mm diameter pipe for area ratio $\sigma = 0.54$ are shown in Fig. 8 as a function of Reynolds number, Re_d. The liquid Reynolds number is defined as

$$\mathrm{Re}_d = Gd/\mu_l$$

where G is the total mass flux corresponding to orifice section, d is the orifice diameter, and μ_l is the viscosity of liquid. It is observed that the static pressure attains the (locally) smallest value at a distance of about $z'/d = 0.5$ after the orifice section and depends only slightly on the mass flow rates. For the same s/d value the axial pressure drop at the orifice section increases with

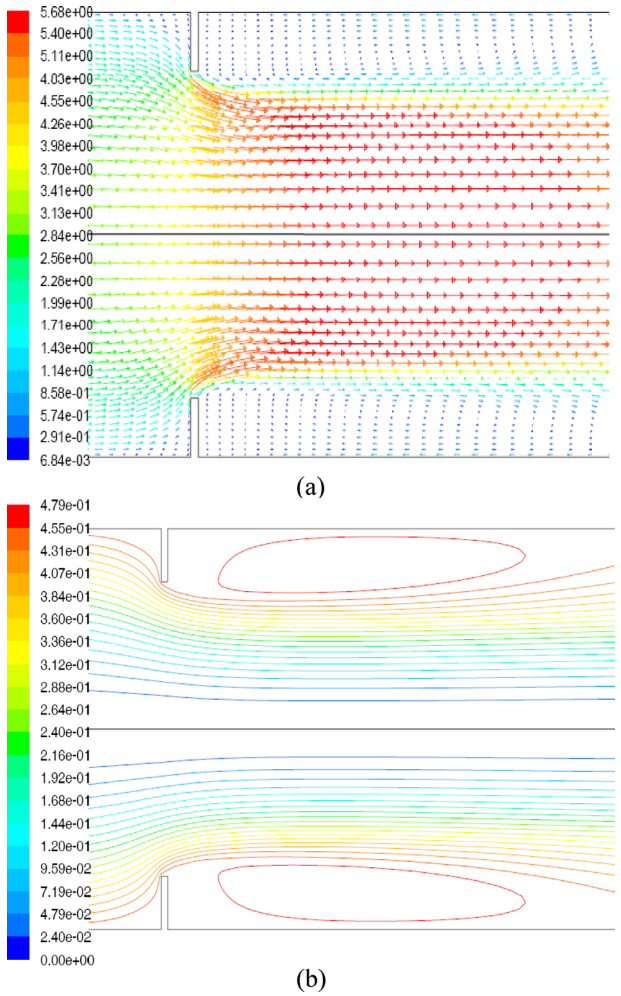

Fig. 5 (*a*) Velocity vectors and (*b*) stream lines for single phase water flow through orifice $\sigma = 0.54$, $s/d = 0.027$, and $D = 40$ mm

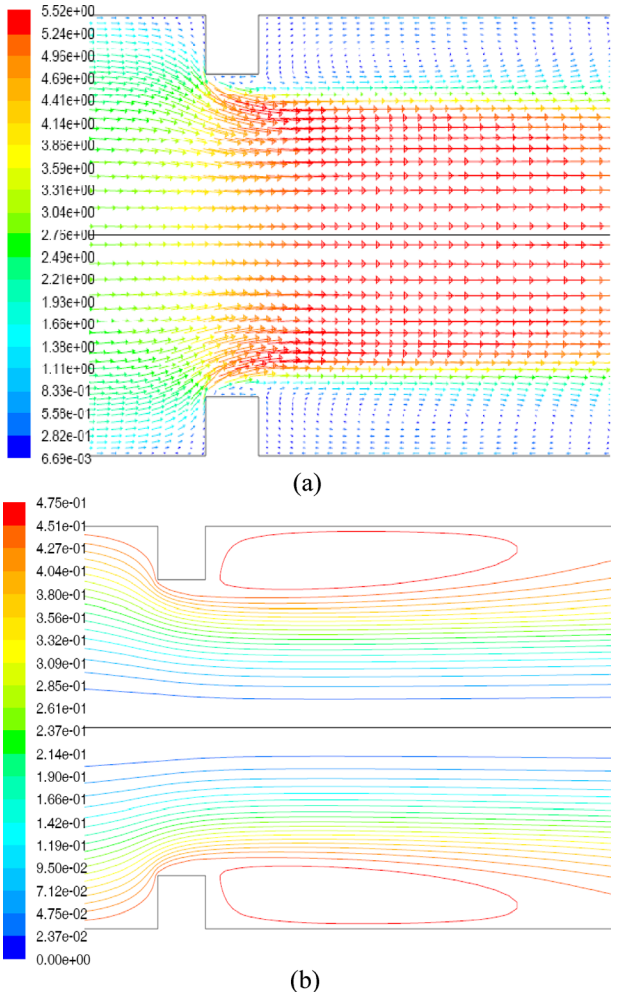

Fig. 6 (*a*) Velocity vectors and (b) stream lines for single phase water flow through orifice $\sigma = 0.54$, $s/d = 0.2$, and $D = 40$ mm

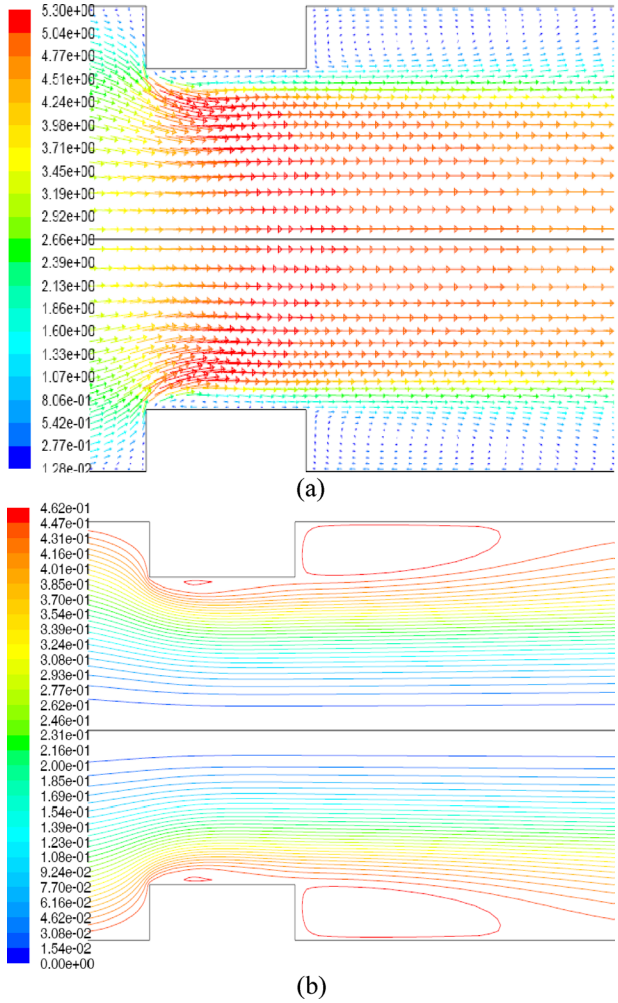

Fig. 7 (*a*) Velocity vectors and (*b*) stream lines for single phase water flow through orifice $\sigma = 0.54$, $s/d = 0.59$, and $D = 40$ mm

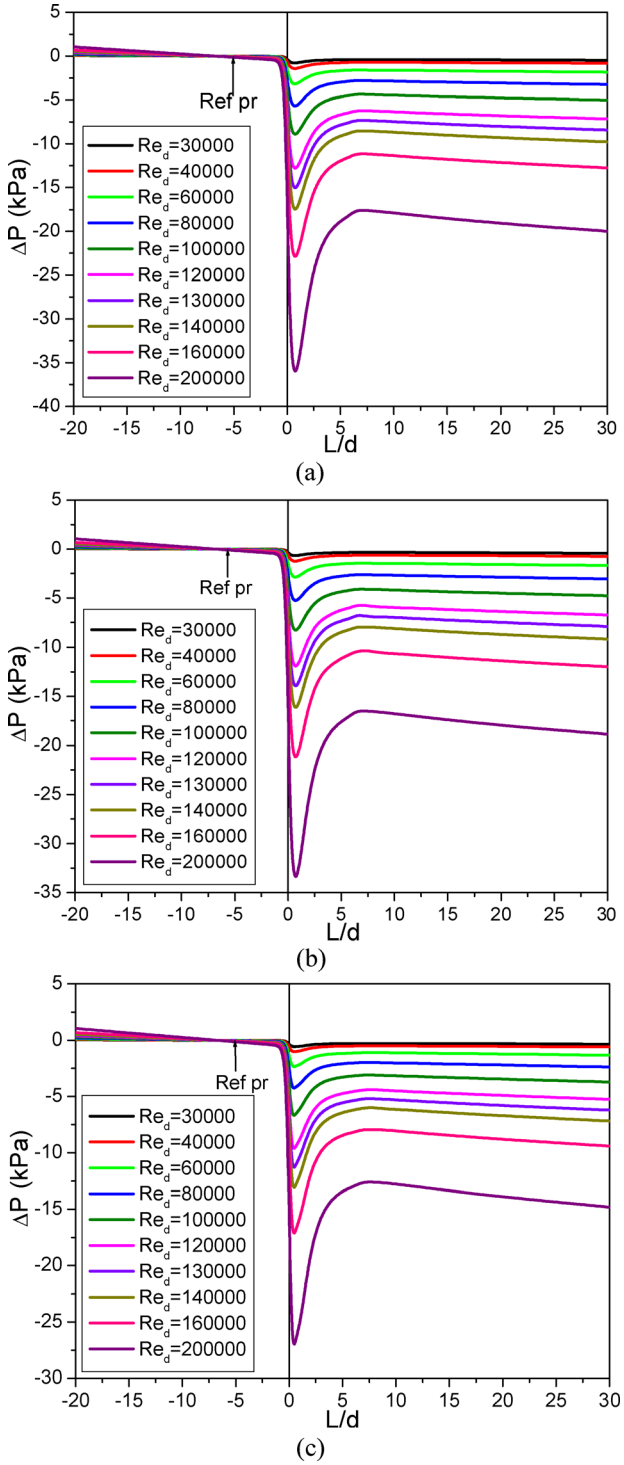

Fig. 8 Pressure profiles for single phase water flow through $D = 40$ mm, $\sigma = 0.54$, (*a*) $s/d = 0.025$, (*b*) $s/d = 0.2$, (*c*) $s/d = 0.59$ orifice

increasing Re_d number. The pressure drop decreases with increasing s/d under the same Re_d number. This may be due to the fact that as thickness of orifices decreases, the recirculation length increases and due to the formation of more vortices, the axial pressure drops at the orifice section increases.

The normalized pressure drops for different Reynolds number for 40 mm diameter pipe having orifice thickness to diameter ratio 0.025 and area ratio 0.54 is shown in Fig. 9. It is evident from Fig. 9 that the normalized pressure drop (i.e., $\Delta P/(\rho v^2/2)$) is independent of Reynolds number. For lower values of Reynolds numbers (i.e., $\mathrm{Re} = 30,000$ and $\mathrm{Re} = 40,000$) the pressure profiles slightly changes with the Reynolds number, whereas for Reynolds numbers above 50000 the normalized pressure profiles exactly merge with each other.

Again by normalizing the pressure drops by $\rho v^2/2$, it is observed that the pressure profiles for 40 mm and 60 mm diameter pipes for same Reynolds number exactly merge with each other as shown in Fig. 10. From Figs. 9 and 10, it can be simply concluded that the normalized pressure drop is independent of Re_d and pipe size.

Figure 11 shows the pressure profile for single phase flow of water through orifices of different thickness for $\mathrm{Re}_d = 200,000$. It clearly shows that the pressure drop, ΔP across the orifice increases with a decrease in orifice thickness and pressure drop decreases with an increase in area ratio. For the same pipe diameter, when the area flow ratio decreases, orifice diameter also decreases. When expansion takes place from smaller diameter to larger diameter, the height of the recirculation zone increases. This results in the formation of more vortices and hence more pressure drop will occur.

From the computed pressure profiles upstream and downstream of the orifice, the local pressure drop has been obtained by extrapolating these profiles to the orifice section. From the local pressure drop values the orifice discharge coefficient C_d is calculated, from which the contraction coefficient σ_c has been obtained by means of Eqs. (3)–(5). Figures 12 and 13, which refer to either the 60 mm or 40 mm diameter pipe show the σ_c values as a function of restriction Reynolds number, Re_d for different values of the

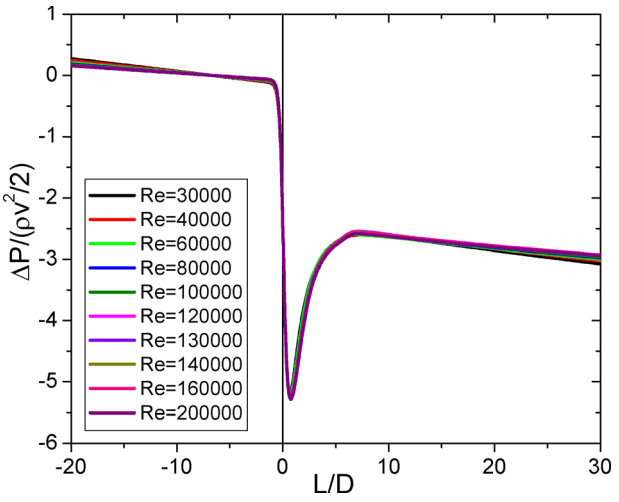

Fig. 9 Normalized axial pressure profile at the orifice section for different Reynolds number ($D = 40$ mm, $\sigma = 0.54$, $s/d = 0.025$)

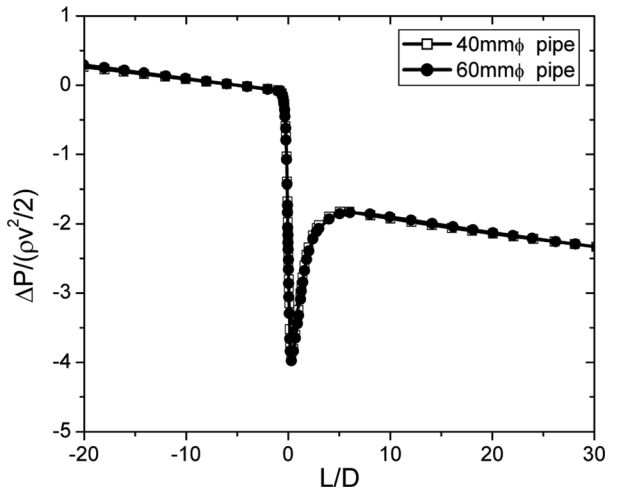

Fig. 10 Normalized axial pressure profile at the orifice section for two different pipes ($\sigma = 0.54$, $s/d = 0.59$, Re = 100,000)

flow area ratio. It can be observed from Figs. 12 and 13 that the contraction coefficient turns out to be independent of the Reynolds number for values above 5×10^4. For lower values of Reynolds number, the contraction coefficient generally increases with it. Finally it can be noticed that the contraction coefficient data are in good agreement with Chisholm formula predictions (Eq. (6)). The contraction coefficient is high (around 0.8) for 0.73 of area flow ratio, whereas that for area flow ratio of 0.54, is around 0.7. This is because for higher area flow ratio, the orifice diameter is more and so the height of the recirculation zone is smaller and hence the pressure drop is less. From Eq. (3) it can be observed that when ΔP less is, C_d is more. From Eq. (4) it can be observed that when C_d is more, σ_c is more.

Figure 14 shows the effect of orifice thickness on the local pressure drop during the single-phase flow. It clearly indicates that the pressure drop across the $s/d = 0.20$ orifice is slightly smaller than that obtained with the $s/d = 0.027$ orifice, even if both orifices can be classified as thin orifices. As a consequence, the contraction coefficient calculated by means of Eq. (4) for the $s/d = 0.20$ orifice is greater than that calculated for the thinner orifices ($s/d \leq 0.05$) as can be seen from Figs. 12 and 13. With turbulent flows through orifices the contraction coefficients are found to be slightly higher for contraction area ratio $\sigma = 0.73$ than that for $\sigma = 0.54$.

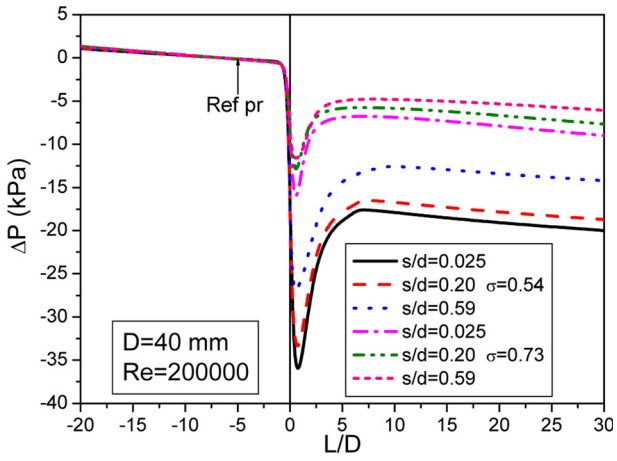

Fig. 11 Pressure profiles for single phase water flow through different orifices ($D = 40$ mm)

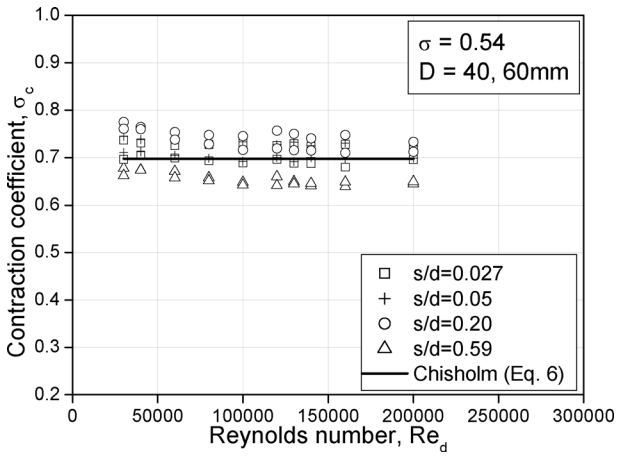

Fig. 12 Contraction coefficient as a function of local Reynolds number for $\sigma = 0.54$

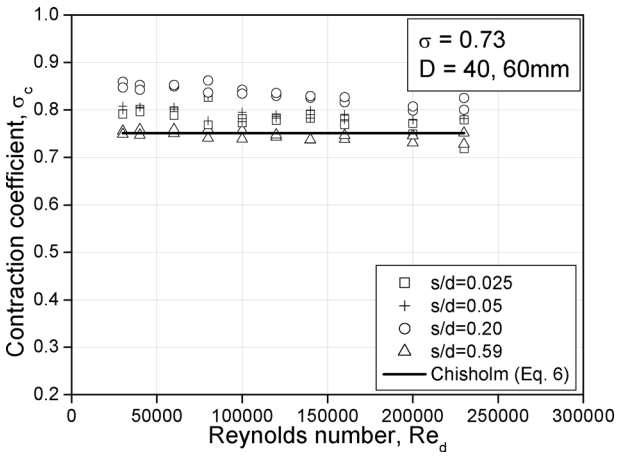

Fig. 13 Contraction coefficient as a function of local Reynolds number for $\sigma = 0.73$

4.2 Two-Phase Flow. The pressure loss due to the contraction occurring during the two-phase flow through the orifice is calculated from computed upstream and downstream pressure gradients. The procedure is based on the assumption that the orifice does not affect the pressure profiles with respect to the unrestricted flow. Pressure profiles for two-phase air-water flow

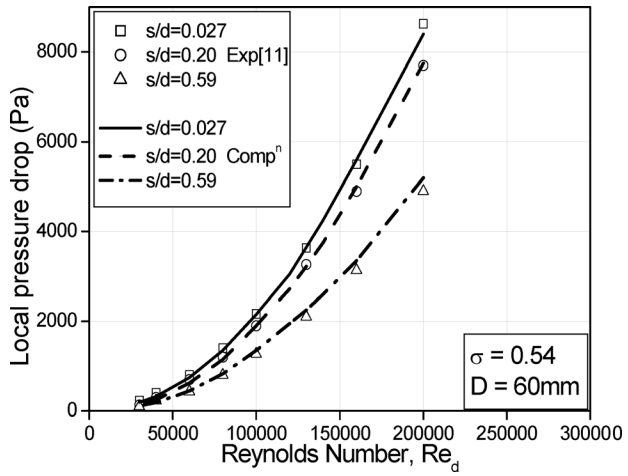

Fig. 14 Single-phase pressure drop as a function of local Reynolds number for $\sigma = 0.54$

through the orifice having $s/d = 0.2$ in 40 mm diameter pipe for $\sigma = 0.54$ and $\sigma = 0.73$ are shown in Figs. 15(*a*) and 15(*b*), respectively, for a constant superficial velocity of water and different superficial velocity of air. It can be observed that the pressure drop increases with increasing the volume fractions of air. The same trend is observed for the flow through 60 mm diameter pipe. Typical pressure drop values as a function of gas and liquid superficial velocities are shown in Figs. 16(*a*) and 16(*b*) where corresponding experimental (Fossa and Guglielmini [11]) values have been plotted in the same graph. It can be marked from Fig. 16 that the agreement between the computation and the experimental values are pretty nice especially taking into account the complicated CFD equations those have been used to compute the pressure profiles in the present computation. It can also be observed that the effect of the orifice thickness on pressure drop is stronger with the orifice of the area flow ratio $\sigma = 0.73$, while the pressure drops across the orifice of the area ratio $\sigma = 0.54$ through different orifice thicknesses are always comparable, with deviations less than 15%. Further it can be noticed that pressure drop increases with a decrease in orifice thickness irrespective of the area ratios.

The singular two-phase multiplier φ_{lo}^2 has been obtained by comparison with single phase computed pressure drops considering only liquid flow. The results are shown in Figs. 17(*a*) and 17(*b*) with reference to the restrictions having $\sigma = 0.54$ and in Figs. 18(*a*) and 18(*b*) that refer to the larger area flow ratio constrictions of $\sigma = 0.73$. All these figures contain the data for both 60 mm inner diameter pipe (empty symbols) and the 40 mm inner diameter pipe (filled symbols). The numerical results for two phase multiplier are compared with the predictions of the homogeneous model (Eq. (12)), and with the values calculated by the relationships of Chisholm for thick orifices (Eq. (13)

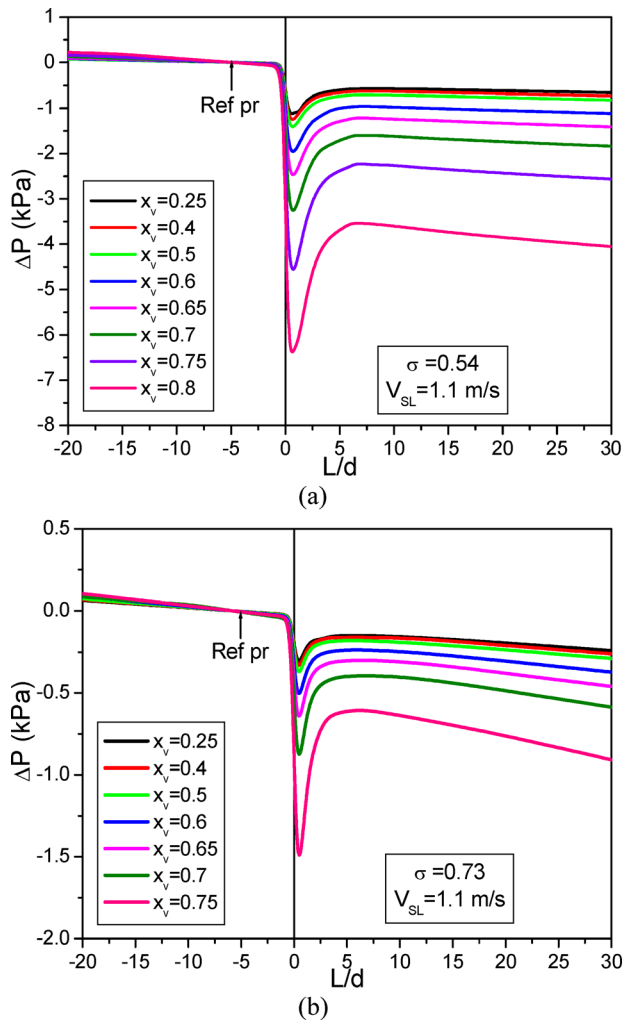

Fig. 15 Pressure profiles for two-phase air-water flow through $D = 40$ mm, $s/d = 0.2$, (*a*) $\sigma = 0.54$, (*b*) $\sigma = 0.73$ orifice

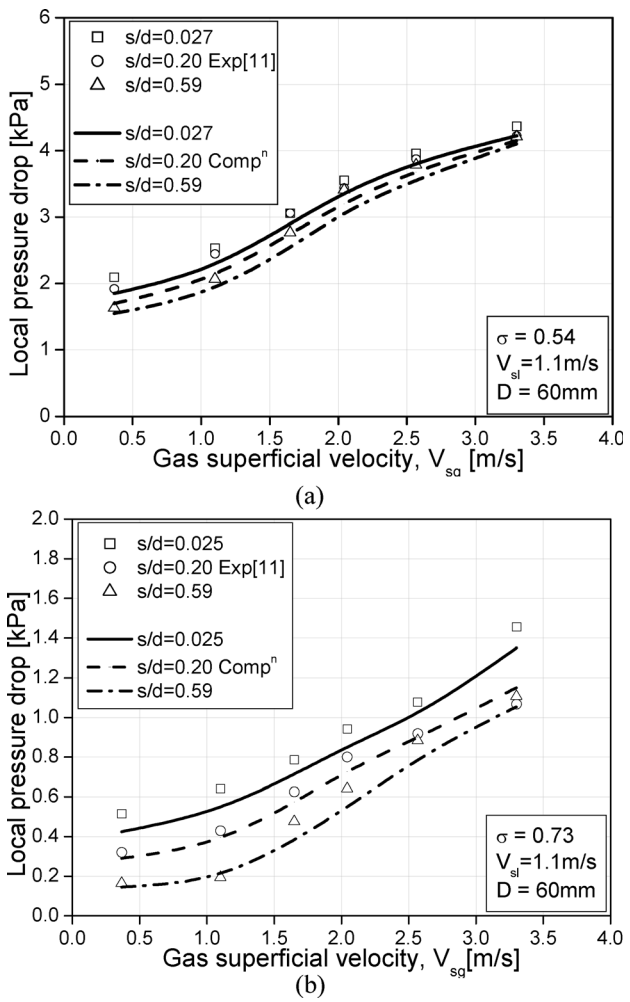

Fig. 16 Local pressure drop as a function of gas superficial velocity and orifice thickness (*a*) $\sigma = 0.54$, (*b*) $\sigma = 0.73$

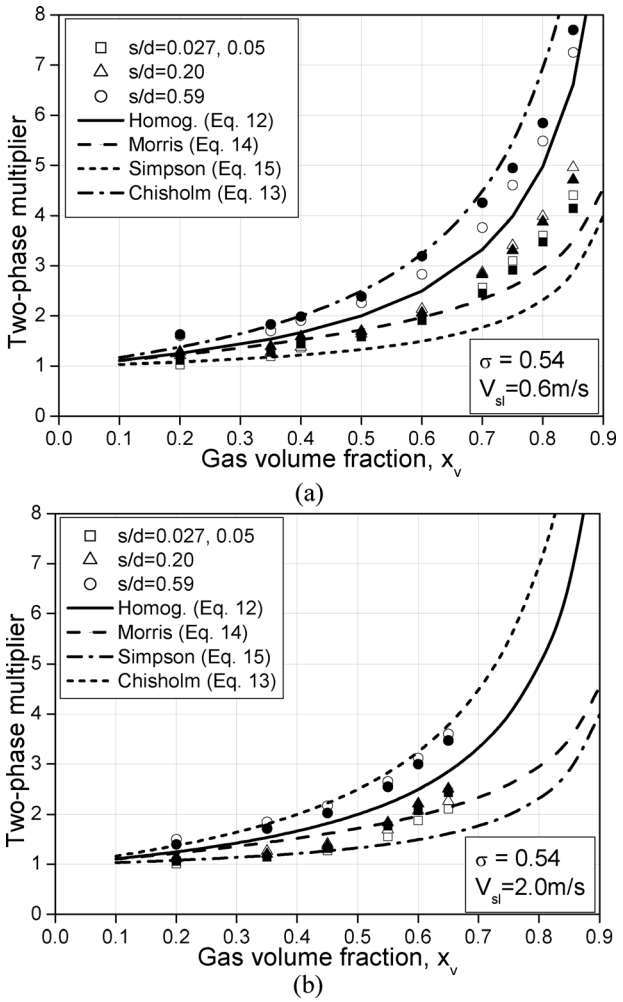

Fig. 17 Pressure multiplier versus gas volume fraction for different orifice thickness, $\sigma = 0.54$ (*a*) $V_{sl} = 0.6$ m/s, (*b*) $V_{sl} = 2.0$ m/s (filled symbols for $D = 40$ mm, empty symbols for $D = 60$ mm)

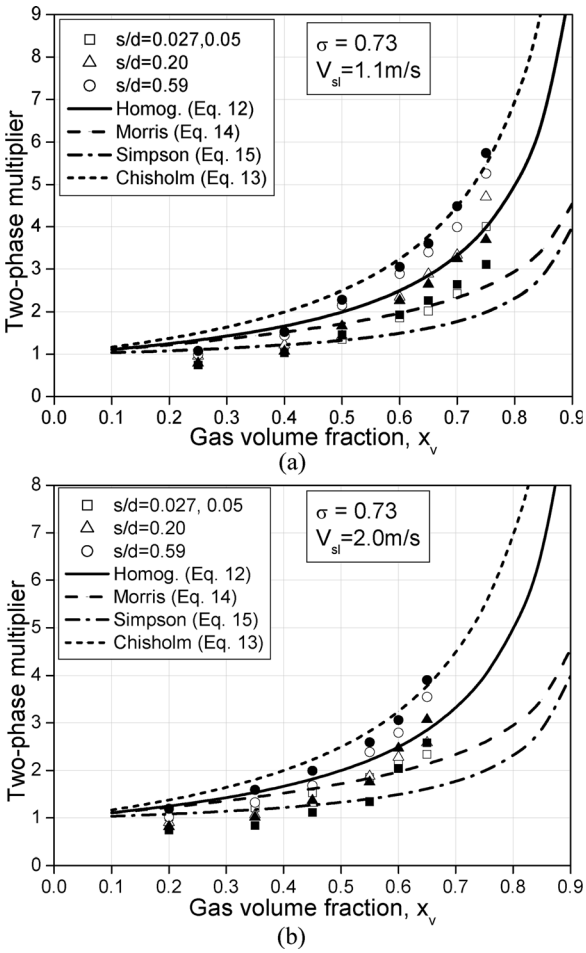

Fig. 18 Pressure multiplier versus gas volume fraction for different orifice thickness, $\sigma = 0.73$ (*a*) $V_{sl} = 1.1$ m/s, (*b*) $V_{sl} = 2.0$ m/s (filled symbols for $D = 40$, empty symbols for $D = 60$ mm)

with $B = 1.5$), Morris (Eqs. (7) and (14)) and Simpson et al. (Eqs. (11) and (15)). The two-phase multiplier for thin orifices ($s/d = 0.025$–0.2) are found to be quite well correlated by Morris equation. Thicker orifices ($s/d = 0.59$) are characterized by higher pressure multipliers whose values are quite well fitted by the proper Chisholm formula. It can be observed from Fig. 18, the pressure multipliers pertinent to the area ratio of $\sigma = 0.73$ show values close to unity (or even lower) when the gas volume fraction is less than about 0.5. No available relationships can account for this effect, which seems to be peculiar to these moderate flow area restrictions. The Saadawi et al. relationship (Eq. (16)) has been discarded from the present comparisons due to the fact it under predicts the numerical as well as the experimental values with differences even greater than 100%.

The main conclusion from pressure multiplier analysis is that the influence of liquid flow rate is weak. Furthermore, it can be observed that the dimensionless pressure drops obtained for $s/d \leq 0.20$ (thin orifices) result in a narrow range of values. The thicker orifices ($s/d = 0.59$) are characterized by higher pressure multipliers, which can show values higher than those predicted by the homogeneous model (Eq. (12)). This occurrence can be mainly ascribed to the fact that as the restriction thickness increases (up to "thick orifice" values), the single-phase pressure drops decrease much more than the two-phase pressure drops increase at the same liquid flow rate (Fig. 14 and Figs. 16(*a*) and 16(*b*)). The numerical results pertinent to thick orifices are quite well fitted by Chisholm formula (Eq. (13) with $B = 1.5$), which account for orifice thickness. Finally it is evident that the pipe diameter has very little effect on the two-phase multiplier.

Figure 19 shows the typical void fraction profiles along the pipe upstream and downstream of the orifices of different thicknesses and different area ratios. The analysis of the void fraction profiles reveals that the void fraction generally undergoes a step change across the orifice with a sharp increase just downstream of the orifice. The results show that the void fraction usually attains a maximum value at a distance of around 0.5 diameters from the throat. The maximum void fraction can be up to twice the value recorded far from the orifice in the upstream direction (in the region of fully developed flow). This maximum value of void fraction is more in orifices having lower contraction area ratio ($\sigma = 0.54$) than that in higher area ratio ($\sigma = 0.73$). The average void fraction increases after the flow passes the orifice. This may be due to the fact that after the vena contracta the flow expands and the flow takes place against adverse pressure gradient. It has been observed that the slip ratio generally attains its minimum value just downstream of the orifice. So, the gas phase velocity decreases and hence there will be increase in void fraction just downstream of the orifice. When the area ratio decreases, orifice diameter also decreases and when expansion occurs from smaller diameter to the larger diameter, the height of the recirculation zone increases. This result in the formation of more vortices and hence average void fraction behind orifices for area flow ratios of 0.54 is more than that for area flow ratios of 0.73. This behavior has been observed irrespective of the orifice thickness for the higher values of the liquid flow rate ($V_{sl} = 1.1$, 2.0 m/s). At $V_{sl} = 0.6$ m/s for ($\sigma = 0.73$) the void fraction profiles exhibit a

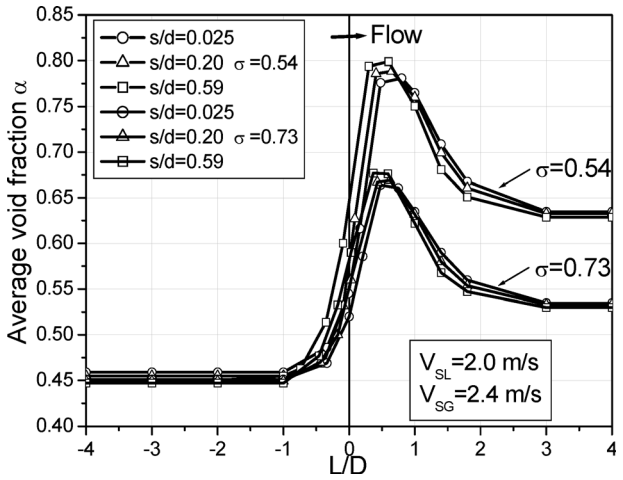

Fig. 19 Average void fraction along the pipe ($D = 40$ mm) for different orifice thickness and area ratio

different pattern with slight changes across the restriction and even, in some operating conditions, a reduction of the void fraction at $(z'/D = 0.5)$ with respect to the preceding measuring location $(z'/D = -2)$.

From void fraction values, the slip ratio profiles have been obtained as a function of gas and liquid flow rates. The numerical results are compared with some available correlations, namely Armand and Treschev (Eq. (9)), Chisholm (Eq. (7)), and Simpson (Eq. (11)). It is worth noticing that Eq. (7) provides good agreement with the numerical results. Figures 20(*a*) and 20(*b*) show some results for slip ratios obtained with restrictions having $\sigma = 0.54$ for 60 mm diameter pipe. The figures indicate that the slip ratio generally attains its minimum values just downstream of the orifice. In such location, the slip ratio can even be less than homogeneous flow values. Far from the orifice, the numerical results are well fitted by both Chisholm and Armand correlations. Finally, it can be noticed that Simpson et al. correlation always overpredicts the data, which explains the poor reliability of the pressure multiplier correlation proposed by the same authors. Figures 21(*a*) and 21(*b*) refer to the 40 mm diameter pipe with restrictions having area ratio $\sigma = 0.73$ and also show slip ratio values just upstream of the orifice. At $(z'/D = -2)$ the slip ratio is greater than that in the immediately downstream of the orifice $(z'/D = 0.5)$. Moreover the slip ratio downstream of the orifice is found to be decreasing with increase in gas flow rate. This is due to the fact that the increase in the gas volume fraction, x_v enhances the phase interactions across the orifice resulting in a slip ratio decrease just downstream of the restriction. The influences of the orifice thickness on slip ratio appears to be weak especially far from the restriction and only at $z'/D = 0.5$ some differences are

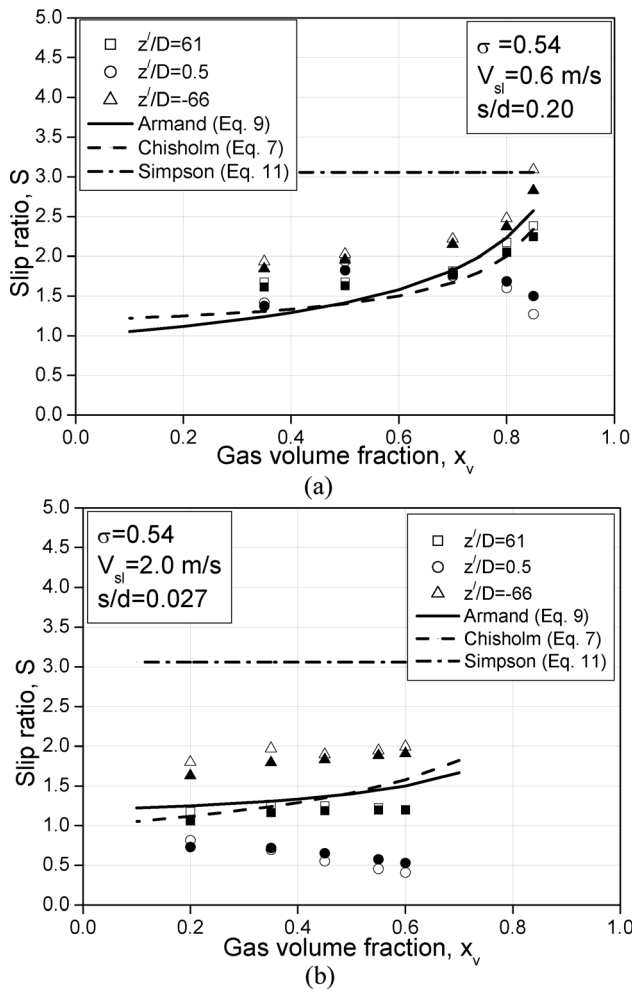

Fig. 20 Slip ratio as a function of gas volume fraction at different location for $\sigma = 0.54$ and $D = 60$ mm (filled symbols Expt. [11], empty symbols computation), (*a*) $V_{sl} = 0.6$ m/s, (*b*) $V_{sl} = 2.0$ m/s

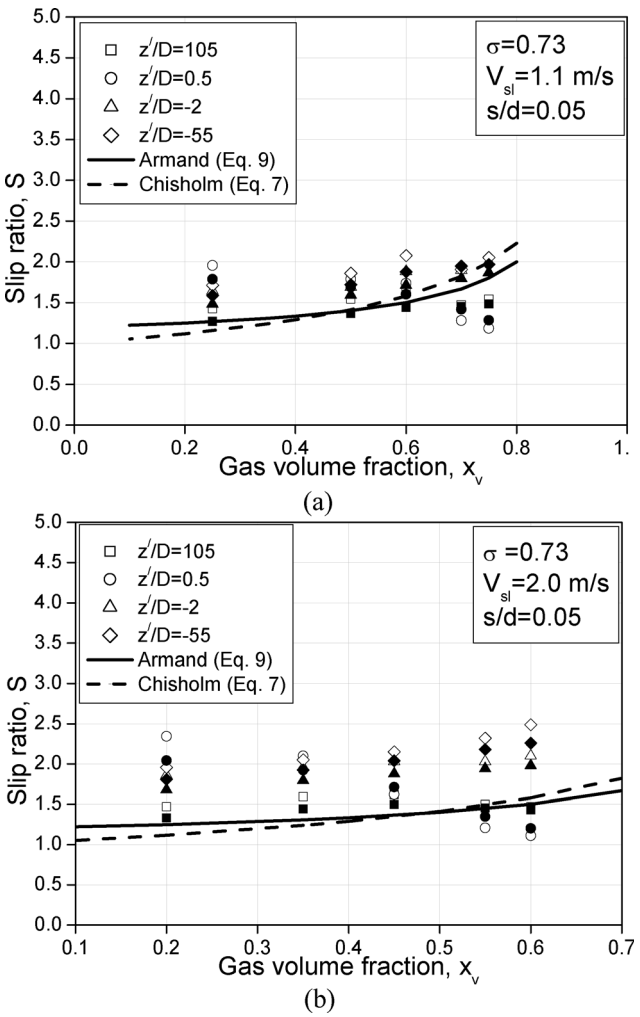

Fig. 21 Slip ratio as a function of gas volume fraction at different location for $\sigma = 0.73$ and $D = 40$ mm (filled symbols Expt. [11], empty symbols computation), (*a*) $V_{sl} = 1.1$ m/s, (*b*) $V_{sl} = 2.0$ m/s

observed in void fraction values and hence in slip ratio values. The slip ratio generally increases slightly with increasing the orifice thickness.

5 Conclusions

A mathematical model for the flow through thin and thick orifices in horizontal pipes with air–water mixtures has been developed by using two-phase flow model in an Eulerian scheme in this study. The major observations made relating to the pressure drop, void fraction and slip ratio values in the process of flow through orifices, can be summarized as follows:

- The contraction coefficient is found to be independent of the Reynolds number for values above 5×10^4. With turbulent flow through orifices the contraction coefficients for single phase flow of water are found to be slightly higher for contraction area ratio $\sigma = 0.73$ than that for $\sigma = 0.54$.
- In single-phase flow the contraction coefficient is found to be in good agreement with the experimental data [11] as well as with the Chisholm [3] formula predictions. The computed pressure drop across the orifice having thickness to diameter ratio, $s/d = 0.20$ is slightly less than that obtained with the $s/d = 0.025$, and $s/d = 0.05$ orifices, even though all these restrictions can be classified as thin orifices.
- The two-phase multiplier for thin orifices ($s/d = 0.025$ to 0.2) are found to be quite well correlated by Morris equation. Thicker orifices ($s/d = 0.59$) are characterized by higher pressure multipliers whose values are quite well fitted by the proper Chisholm formula. Finally, the two-phase multipliers pertinent to the orifice having area ratio $\sigma = 0.73$ show values close to unity (or even lower) when the gas volume fraction is less than about 0.5. The pipe diameter has very little effect on the two-phase multiplier.
- The time average void fraction generally increases across the orifice and attains the maximum value just downstream of the restriction. The results show that the void fraction usually attains a maximum value at a distance of around 0.5 diameters from the throat. The maximum void fraction can be up to twice the value recorded far from the orifice in the upstream direction (in the region of fully developed flow) and the corresponding slip ratio decreases to values less than 0.5. This behavior has been observed irrespective of the orifice thickness for the higher values of the liquid flow rate and it is more evident for low area ratio ($\sigma = 0.54$).
- The slip ratio generally attains its minimum value just downstream of the orifice, even less than that of the homogeneous flow predictions. Far from the restriction, the numerical results are well fitted by both Chisholm and the Armand correlations. It is found that the Simpson et al. correlation for both slip ratio values as well as two-phase multiplier is not reliable.

Nomenclature

A = flow area (m^2)
C_D = drag coefficient
D = pipe diameter (m)
d = orifice diameter (m)
$\vec{g}$ = acceleration due to gravity (m/s^2)
k = turbulent kinetic energy
$\dot{m}$ = mass flow rate (kg/s)
P = pressure (Pa)
ΔP = pressure drop
Re_d = Reynolds number corresponding to orifice diameter
S = slip ratio
s = orifice thickness (m)
V = velocity (m/s)
V_{sg} = superficial gas velocity (m/s)
V_{sl} = superficial liquid velocity (m/s)
x = mixture quality
x_v = gas volume fraction ($x_v = V_{sg}/(V_{sg}+V_{sl})$)
z = distance from inlet section (m)
z' = distance from restriction (m)

Greek Symbols

α = void fraction
ε = dissipation rate of turbulent kinetic energy
μ = viscosity (kg/ms)
μ_l = laminar viscosity
μ_t = turbulent viscosity
μ^{eff} = effective viscosity
Φ_{lo}^2 = two-phase multiplier
ρ = density (kg/m^3)
σ = area ratio ($\sigma = (d/D)^2$)
σ_c = contraction coefficient
σ_k = turbulent Prandtl number for k
σ_ε = turbulent Prandtl number for ε
$\bar{\bar{\tau}}$ = stress tensor
$\vec{v}$ = velocity vector

Subscripts

C = vena contracta
g = gas
l = liquid
p = secondary phase
q = primary phase

References

[1] Idelchik, I. E., Malyavskaya, G. R., Martynenko, O. G., and Fried, E., 1994, *Handbook of Hydraulic Resistances*, CRC Press, Boca Raton.
[2] Simpson, H. C., Rooney, D. H., and Grattan, E., 1983, ''Two-Phase Flow Through Gate Valves and Orifice Plates," Proceedings of the International Conference on Physical Modelling of Multi-Phase Flow, Coventry.
[3] Chisholm, D., 1983, *Two-Phase Flow in Pipelines and Heat Exchangers,* Longman Group Ed., London.
[4] Morris, S. D., 1985, "Two Phase Pressure Drop Across Valves and Orifice Plates," Proceedings of the European Two Phase Flow Group Meeting, Marchwood Engineering Laboratories, Southampton, UK.
[5] Friedel, L., 1984, "Two-Phase Pressure Drop Across Pipe Fitting," HTFS Report No. RS41.
[6] Janssen, E., 1966, "Two-Phase Pressure Loss Across Abrupt Area Contractions and Expansions: Steam Water at 600 to 1400 PSIA," Proceedings of the 3rd International Heat Transfer Conference, Chicago, IL, Vol. 5, pp. 13–23.
[7] Lin, Z. H., 1982, "Two Phase Flow Measurement With Sharp Edge Orifices," Int. J. Multiphase Flow, **8**, pp. 683–693.
[8] Saadawi, A. A., Grattan, E., and Dempster, W. M., 1999, "Two Phase Pressure Loss in Orifice Plates and Gate Valves in Large Diameter Pipes," Proceedings of the 2nd Symposium on Two-Phase Flow Modelling and Experimentation, G. P. Celata, P. D. Marco, R. K. Shah, eds., ETS, Pisa, Italy.
[9] Kojasoy, G., Kwame, M. P., and Chang, C. T., 1997, "Two-Phase Pressure Drop in Multiple Thick and Thin Orifices Plates," Exp. Thermal Fluid Sci., **15**, pp. 347–358.
[10] Bertola, V., 2004, "The Structure of Gas–Liquid Flow in a Horizontal Pipe With Abrupt Area Contraction," Exp. Thermal Fluid Sci., **28**, pp. 505–512.
[11] Fossa, M., and Guglielmini, G., 2002, "Pressure Drop and Void Fraction Profiles During Horizontal Flow Through Thin and Thick Orifices," Exp. Thermal Fluid Sci., **26**, pp. 513–523.
[12] Fossa, M., Guglielmini, G., and Marchitto, A., 2006, "Two-Phase Flow Structure Close to Orifice Contractions During Horizontal Intermittent Flows," Int. Commun. Heat Mass Transfer, **33**, pp. 698–708.
[13] Jones, O. C., and Zuber, N., 1975, "The Interrelation Between Void Fraction Fluctuations and Flow Patterns in Two-Phase Flow," Int. J. Multiphase Flow, **2**(3), pp. 273–306.
[14] Shedd, T. A., and Newell, T. A., 2004, "Characteristics of the Liquid Film and Pressure Drop in Horizontal, Annular, Two-Phase Flow Through Round, Square and Triangular Tubes," ASME J. Fluids Eng., **126**(5), pp. 807–817.
[15] Grace, H. P., and Lapple, C. E., 1951, "Discharge Coefficient of Small Diameter Orifices and Flow Nozzles," Trans. ASME, **73**, pp. 639–647.
[16] Bullen, P. R., Cheeseman, D. J., Hussain, L. A., and Ruffel, A. E., 1987, "The Determination of Pipe Contraction Coefficients for Incompressible Turbulent Flow," Int. J. Heat Fluid Flow, **8**, pp. 111–118.
[17] Benedict, R. P., 1980, *Fundamentals of Pipe Flow*, Wiley–Interscience, New York.
[18] Collier, J. G., and Thome, J. R., 1994, *Convective Boiling and Condensation*, Oxford University Press, New York.

[19] Armand, A. A., and Treschev, G., 1947, "Investigation of the Resistance During Movement of the Steam–Water Mixtures in Heated Boiler Pipe at High Pressure," Izvestia Vses. Teplo. Inst. AERE Lib/Trans., **816**(4), pp. 1–5.
[20] Drew, D. A., 1983, "Mathematical Modeling of Two-Phase Flows," Annu. Rev. Fluid Mech., **15**, pp. 261–291.
[21] Drew, D., and Lahey, R. T., Jr., 1979, "Application of General Constitutive Principles to the Derivation of Multidimensional Two-Phase Flow Equations," Int. J. Multiphase Flow, **7**, pp. 243–264.
[22] Crowe, C., Sommerfeld, M., and Tsuji, Y., 1998, *Multiphase Flows With Droplets and Particles*, CRC Press, Boca Raton.
[23] Wallis, G. B., *One-Dimensional Two-Phase Flow*, McGraw-Hill, New York.
[24] Launder, B. E., and Spalding, D. B., 1974, "The Numerical Computation of Turbulent Flows," Comput. Methods Appl. Mech. Eng., **3**, pp. 269–289.
[25] Shih, T. H., Liou, W. W., Shabbir, A., Yang, Z., and Zhu, J., 1995, "A New k-ε Eddy-Viscosity Model for High Reynolds Number Turbulent Flows," Comput. Fluids, **24**(3), pp. 227–238.
[26] Troshko, A. A., and Hassan, Y. A., 2001, "A Two-Equation Turbulence Model of Turbulent Bubbly Flows," Int. J. Multiphase Flow, **27**, pp. 1965–2000.
[27] Wolfstein, M., 1969, "The Velocity and Temperature Distribution of One-Dimensional Flow With Turbulence Augmentation and Pressure Gradient," Int. J. Heat Mass Transfer, **12**, pp. 301–318.
[28] Chen, H. C., and Patel, V. C., 1988, "Near-Wall Turbulence Models for Complex Flows Including Separation," AIAA J., **26**(6), pp. 641–648.
[29] Patankar, S. V., 1980, *Numerical Heat Transfer and Fluid Flow*, McGraw-Hill, Hemisphere, Washington, D.C.
[30] Vasquez, S. A., and Ivanov, V. A., 2000, "A Phase Coupled Method for Solving Multiphase Problems on Unstructured Meshes," Proceedings of the ASME Fluids Engineering Division Summer Meeting (FEDSM2000), FED, Boston, MA, Vol. 251, pp. 659–664.
[31] Ansari, M. R., and Shokri, V., 2007, "New Algorithm for the Numerical Simulation of Two-Phase Stratified Gas–Liquid Flow and Its Application for Analyzing the Kelvin–Helmholtz Instability Criterion With Respect to Wave Length Effect," Nucl. Eng. Design, **237**, pp. 2302–2310.
[32] Wesseling, P., 1992, *An Introduction to Multigrid Methods*, Wiley, UK.
[33] Weiss, J. M., Maruszewski, J. P., and Smith, W. A., 1999, "Implicit Solution of Preconditioned Navier–Stokes Equations Using Algebraic Multigrid," AIAA J., **37**(1), pp. 29–36.